

# High-Output Micro-Machined Electrostatic Actuators

Amin Abbasalipour (✉ [amin.abbasalipour@utdallas.edu](mailto:amin.abbasalipour@utdallas.edu))

University of Texas at Dallas

Prithviraj Palit

University of Texas at Dallas

Sepehr Sheikhlari

University of Texas at Dallas

Siavash Pakdelian

University of Massachusetts

Siavash Pourkamali

University of Texas at Dallas

---

## Article

**Keywords:** MEMS, electrostatic actuator, energy density, cellular actuator, out of plane displacement, submicron transduction gap.

**Posted Date:** June 2nd, 2021

**DOI:** <https://doi.org/10.21203/rs.3.rs-478106/v1>

**License:**  This work is licensed under a Creative Commons Attribution 4.0 International License.

[Read Full License](#)

---

# HIGH-OUTPUT MICRO-MACHINED ELECTROSTATIC ACTUATORS

*Abstract*—This work presents a new class of micromachined electrostatic actuators capable of producing output force and displacement unprecedented for MEMS actuators. The actuators feature submicron high aspect ratio transduction gaps lined up in two-dimensional arrays inspired by the cellular structure of animal muscle tissue. Such arrangement of micro-scale actuator cells, allows addition of force and displacements of a large number of cells (up to 7600 in one array demonstrated), leading to displacements in the hundreds of microns range and several gram-forces of axial force. For 50  $\mu\text{m}$  thick actuators with horizontal dimensions in the 1-4 millimeters range, out of plane displacement of up to 678  $\mu\text{m}$ , bending moment of up to 2.0  $\mu\text{Nm}$  i.e. 0.08 N (~8 gram-force) of axial force over the 50  $\mu\text{m}$  by 2 mm cross-sectional area of the actuator (800 kPa of electrostatically generated stress), and energy density (mechanical work output per stroke per volume) up to 1.42  $\text{mJ}/\text{cm}^3$  have been demonstrated for the actuators.

*Index Terms*—MEMS; electrostatic actuator; energy density; cellular actuator; out of plane displacement; submicron transduction gap.

## INTRODUCTION

Electromechanical actuators converting electrical energy into mechanical force or motion are an integral part of any electrically powered system with moving parts. Examples of such systems with sub-centimeter dimensions include micro-robots<sup>1</sup>, precision positioning systems<sup>2</sup>, optical systems<sup>3</sup>, and medical devices<sup>4</sup>, etc. For such applications, the actuator is required to provide displacements ranging from tens of micrometers to millimeters and supply forces in the mN range. Batch-fabricated micromachined (MEMS) actuators can provide low-cost highly integrated solutions for such applications. However, none of the existing micromachined actuators can meet such large energy output requirements. Transduction mechanisms commonly used in micromachined actuators include electrostatic, piezoelectric, Electro-thermal and electromagnetic. Electromagnetic transduction, which is the main means of electromechanical energy conversion in macro-scale systems, has been conventionally used in smaller scale systems. Such actuators, e.g. voice coil motors (VCM), can produce relatively large force and displacement and are widely used for auto-focus (AF) and optical image stabilization (OIS) in compact camera modules in modern consumer electronics (smart phones, tablets, etc.). However, the need for high-turn coils and magnets makes such actuators hard to miniaturize and batch fabricate via

micromachining. They are also not power efficient due to the need for significant current flow in the coils, potentially even when the actuator is not moving<sup>5</sup>. Piezoelectric actuators on the other hand are highly power efficient and provide high output force, but very small stroke necessitating aggressive leverage mechanisms to reach adequate displacements<sup>6,7,8</sup> at the cost of lowering the force. Furthermore, since inclusion of piezoelectric materials in micromachining processes is mainly limited to thin films, reaching large overall actuator active layer size and therefore high energy output is very challenging if not impossible. Finally, electro-thermal microactuators utilizing thermal expansion and contraction of heated elements can produce large force and displacement (with leverage) but their high-power consumption is prohibitive for most applications<sup>9,10</sup>.

Electrostatic actuators on the other hand are highly power efficient and compatible with semiconductor manufacturing processes. Electrostatic transducers, while barely ever used for power conversion in macroscale systems, are widely used in micro-electro-mechanical systems (MEMS). Examples of such include vibratory gyroscopes<sup>11</sup>, accelerometers<sup>12</sup>, MEMS silicon oscillators<sup>13</sup>, and capacitive micromachined ultrasonic transducers (CMUT)<sup>14</sup>. What makes electrostatic transducers suitable for microscale systems is the fact that narrow air-gaps with sizes in the few microns range can withstand much higher

78 electric fields, compared to larger air-gaps,  
79 without breakdown. According to Paschen's  
80 law<sup>15</sup>, airgaps in the few microns range and  
81 below can withstand extremely large electric  
82 fields (hundreds of MV/m as opposed to 3  
83 MV/m for millimeter scale gaps) without  
84 breakdown<sup>16,17</sup>. Stored energy density in such  
85 electric fields can therefore even surpass 1.0  
86 J/cm<sup>3</sup>, i.e. 20X higher energy density than in  
87 animal muscles. Electrostatic actuators with  
88 air-gaps can also provide displacements in the  
89 few microns range without the need for leverage  
90 mechanisms. This along with the ability to  
91 expand in three dimensions (into the bulk of the  
92 substrate as opposed piezoelectric thin films)  
93 makes electrostatic actuators an interesting  
94 option for achieving high output actuation.

95 Nonetheless, reaching displacement range  
96 of hundreds of microns with output force in the  
97 mN range for micromachined electrostatic  
98 actuators, and to compete with the voice coil  
99 motors, is quite challenging. Displacement of a  
100 parallel plate electrostatic actuator is  
101 fundamentally limited to the air-gap size.  
102 Increasing the air-gap leads to significantly  
103 lower output force, or higher operating voltage,  
104 while the giant breakdown electric field  
105 advantage starts to disappear for air-gaps above  
106 10  $\mu\text{m}$  wide. Comb-drive actuators can bypass  
107 this limitation to some extent but offer much  
108 lower energy densities as the transduction only  
109 occurs by the fringing fields at the tip of the  
110 electrodes as opposed to the whole air-gap area.  
111 Inchworm motors represents an interesting  
112 approach to maintain high energy density of  
113 parallel plate actuators while bypassing the  
114 displacement range limitation via a periodic  
115 back and forth motions along with an integrated  
116 locking mechanism<sup>18</sup>. In this manner  
117 displacement from several strokes of the  
118 actuator can be added up reaching a large  
119 overall displacement. Force density of around  
120 2 mN/mm<sup>2</sup> for operation at 110 V, and  
121 maximum in-plane displacement was 124  $\mu\text{m}$ <sup>19</sup>  
122 has been demonstrated for inchworm motors.  
123 The wear and tear of the lock-in mechanism,  
124 possibility of stiction, and limited speed due to  
125 the required periodic back and forth motion are

126 among major limitations for inchworm motors.

127 Out of plane displacement of 28  $\mu\text{m}$  at 80 V  
128 has been demonstrated for a piston style  
129 electrostatic actuator<sup>20</sup>. Such actuator is  
130 essentially a vertically formed large (mm-scale)  
131 comb-drive actuator formed via wafer bonding,  
132 hence the low output energy density of 0.178  
133  $\mu\text{J}/\text{cm}^3$ . Another recent work based on active  
134 bending of cantilevers was focused on getting  
135 large deflections. The actuator class is  
136 fabricated in a CMOS-compatible process, that  
137 allows high deflections even with small  
138 electrode separation. The electrode separation  
139 of the fabricated actuator cells varies between  
140 110 nm to 226 nm and gave static deflection of  
141 226 nm at 45 V. This actuator class allowed  
142 deflection with travel ranges widely beyond the  
143 pull-in limit even very small electrode  
144 separation<sup>21</sup>. In summary, despite significant  
145 potential and efforts, no viable millimeter scale  
146 actuation solutions have been offered by MEMS  
147 electrostatic actuators so far.

148 Inspired by the cellular structure of  
149 biological muscle tissue, the proposed approach  
150 in this work is based on two dimensional arrays  
151 of parallel-plate actuator cells to combine force  
152 and displacement of individual cells achieving  
153 unprecedented range of stroke and output  
154 force<sup>22</sup>.

155 Utilization of the high aspect ratio  
156 polysilicon and single crystalline silicon  
157 (HARPSS)<sup>23</sup> fabrication approach allows  
158 formation of submicron electrostatic  
159 transduction gaps within thick silicon  
160 structures. This leads to large output energy  
161 density for the resulting actuators while  
162 maintaining relatively low actuation voltages.

## 163 RESULTS

### 164 ACTUATOR DESIGN AND OPERATION PRINCIPLE:

165 Each cellular electrostatic actuator is  
166 comprised of an arrangement of individual  
167 parallel plate actuator cells with submicron  
168 transduction air-gaps in large 2-dimensional  
169 suspended arrays. The force and displacement  
170 of individual microscale actuator cells within

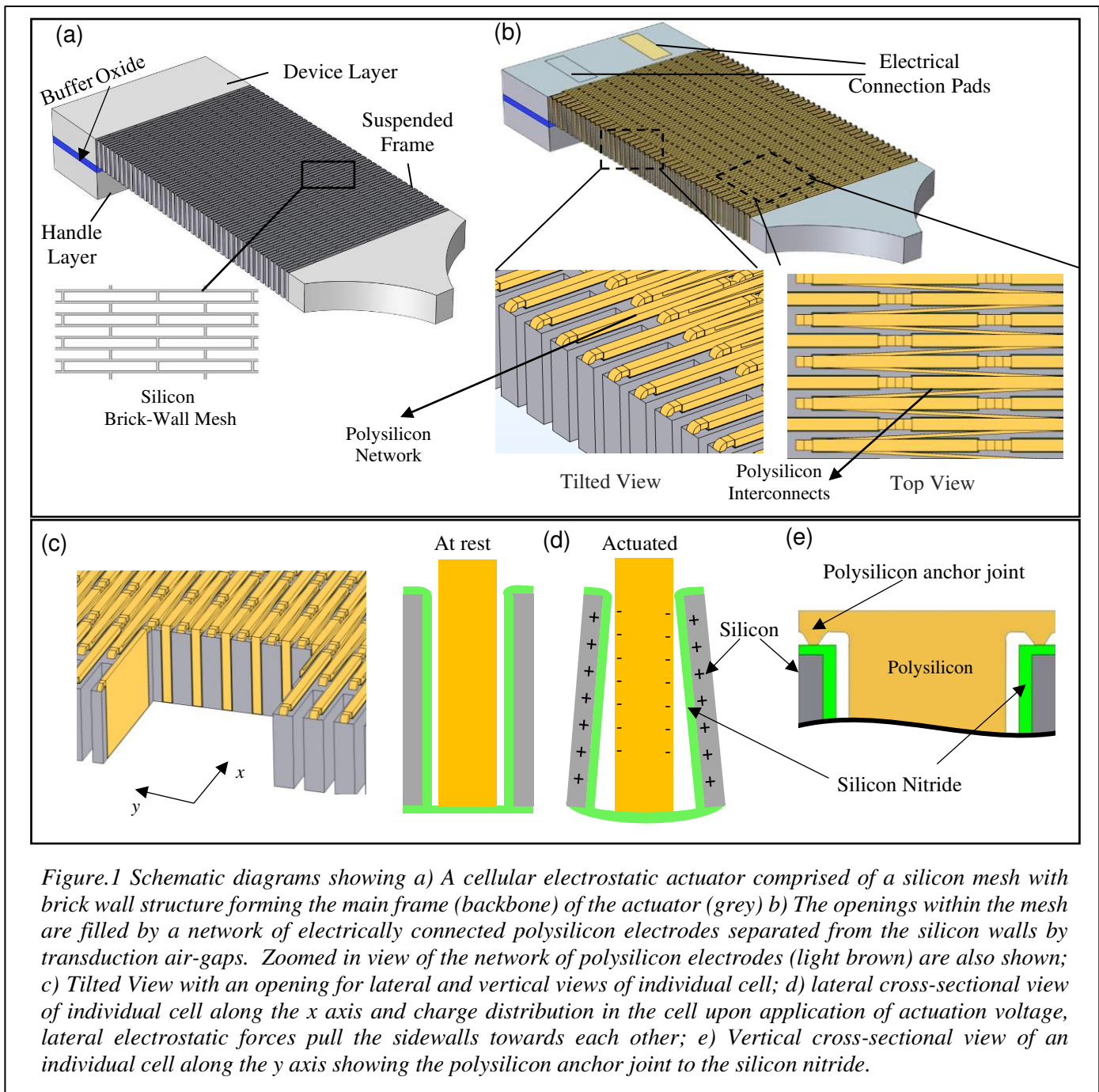


Figure.1 Schematic diagrams showing a) A cellular electrostatic actuator comprised of a silicon mesh with brick wall structure forming the main frame (backbone) of the actuator (grey) b) The openings within the mesh are filled by a network of electrically connected polysilicon electrodes separated from the silicon walls by transduction air-gaps. Zoomed in view of the network of polysilicon electrodes (light brown) are also shown; c) Tilted View with an opening for lateral and vertical views of individual cell; d) lateral cross-sectional view of individual cell along the x axis and charge distribution in the cell upon application of actuation voltage, lateral electrostatic forces pull the sidewalls towards each other; e) Vertical cross-sectional view of an individual cell along the y axis showing the polysilicon anchor joint to the silicon nitride.

171 the array, are added up leading to large actuation  
 172 forces. In an Individual animal muscle, the cells  
 173 have very limited deformation and force output.  
 174 However, millions of cells forming a tissue can  
 175 provide significant displacement and force by  
 176 adding the force and displacement of individual  
 177 cells. Similarly, the force and displacement of  
 178 individual microscale actuator cells integrated  
 179 within the array are added up leading to  
 180 relatively large actuation force and

181 displacement amplitude. Figure 1(a) shows the  
 182 schematic view of a rectangular cellular  
 183 actuator array. The main skeleton (backbone) of  
 184 the actuator is a crystalline silicon conductive  
 185 mesh with moderate stiffness and ability to  
 186 undergo significant strains (tens of percent). In  
 187 this manner even though the actuators are made  
 188 of hard materials, the flexible mesh can be  
 189 designed to mimic functionality and flexibility  
 190 of a soft material with desired stiffness. The

191 openings within the mesh are filled by a  
192 network of another conductive material  
193 (polysilicon in this work) separated from the  
194 actuator walls by narrow actuation air-gaps with  
195 thickness ranging from tens of nanometers to a  
196 few microns. Ultra-narrow tall capacitive gaps  
197 with high aspect ratios are created between the  
198 frame sidewalls and the polysilicon filling the  
199 mesh openings (Figure 1(b)) using a variation of  
200 the High Aspect Ratio Polysilicon and Single  
201 crystalline Silicon (HARPPS) fabrication  
202 technique. The frame (or electrode) sidewalls  
203 are to be covered by a thin dielectric layer to  
204 avoid electrical shorts between electrodes and  
205 the sidewalls upon potential contact. Silicon  
206 nitride has been used in this work for covering  
207 the silicon mesh sidewalls as it is widely  
208 available and compatible with silicon  
209 micromachining. Silicon nitride is known to  
210 help with mechanical reliability by reducing the  
211 possibility of electrode and sidewall surfaces  
212 sticking upon contact. The dielectric layer is  
213 also expected to increase the air-gap breakdown  
214 field by blocking flow of electrons due to field  
215 emission or tunneling<sup>24</sup>.

216 Upon application of the actuation voltage  
217 between the silicon frame and polysilicon  
218 electrodes, the lateral electrostatic forces pull  
219 the sidewalls towards each other leading to  
220 contraction of the whole frame. To achieve out  
221 of plane displacement, the thin film of silicon  
222 nitride that also covers the bottom of the cells,  
223 can be kept on the bottom surface. The  
224 dielectric film locks the two sidewalls on the  
225 bottom preventing them from moving with  
226 respect to each other. Therefore, contraction of  
227 the silicon mesh only occurs on the top portion  
228 of the cells leading to an overall bending  
229 moment curving the actuator and moving its tip  
230 upwards. Each polysilicon electrode is anchored  
231 onto the silicon mesh at nodal locations  
232 (locations with close to zero deformation), i.e.,  
233 the shared sidewalls between two adjacent cells  
234 in the same row, to have adequate stiffness to  
235 pull the silicon walls without getting deformed  
236 or pulled-in (Figure 1(e)).

237 The parallel plate configuration of actuator  
238 cells (as opposed to comb-drive) leads to larger

239 forces and higher energy density. In a parallel  
240 plate electrostatic actuator, displacement range  
241 of the movable electrode is limited to the air-gap  
242 between the electrodes. A tradeoff exists  
243 between the achievable energy density and  
244 operating voltage of such actuators, and the  
245 range of displacement. The array structures can  
246 bypass this limitation and enable realization of  
247 millimeter scale actuators with high energy  
248 density, large displacement, and moderate  
249 operating voltage. The inverse square  
250 dependence of the electrostatic force between  
251 parallel plates especially makes parallel plates  
252 an attractive option for actuators with ultra-  
253 narrow (submicron) transduction gaps. In case  
254 of the parallel plate cells shown, the maximum  
255 achievable deformation of individual cells is  
256 equal to the sum of the two air-gaps, i.e.  $2g_0$ .  
257 The resulting strain in the center of each cell is  
258 the ratio of  $2g_0$  to the total cell width, which  
259 includes the widths of the silicon frame  
260 sidewall, polysilicon electrode, air-gaps, and the  
261 sidewall dielectric films. Only half of the  
262 silicon frame sidewall width on each side of the  
263 cell is considered in the total width calculation  
264 as the cells share the sidewalls and the outer half  
265 of the sidewall should be considered part of the  
266 adjacent cell. The resulting overall maximum  
267 strain for the whole frame is equal to the ratio of  
268 the air-gap to the cell width, i.e. half as much as  
269 strain in the middle of individual cells. This is  
270 due to the arrangement of cells in a brick-wall  
271 pattern where only half of the cells along the  
272 length of the array are aligned with each other.

#### 274 *DEVICE CHARACTERIZATION AND DC TEST:*

275 Actuators with different sizes were  
276 fabricated using a modified HARPPS  
277 fabrication process (described in the “Materials  
278 and Methods section) on a SOI substrate with  
279 device layer thickness of 50  $\mu\text{m}$ . Actuator array  
280 horizontal dimensions include 2 mm  $\times$  1 mm, 2  
281 mm  $\times$  2 mm and 4 mm  $\times$  2 mm.

282 Figure 2(a) shows scanning electron microscope  
283 (SEM) view of a fabricated 4 mm along 2 mm  
284 wide actuator array consisting of 362 rows and  
285 20 and 21 cells per row in alternative rows (a  
286 total of 7600 cells). Zoomed in views of the

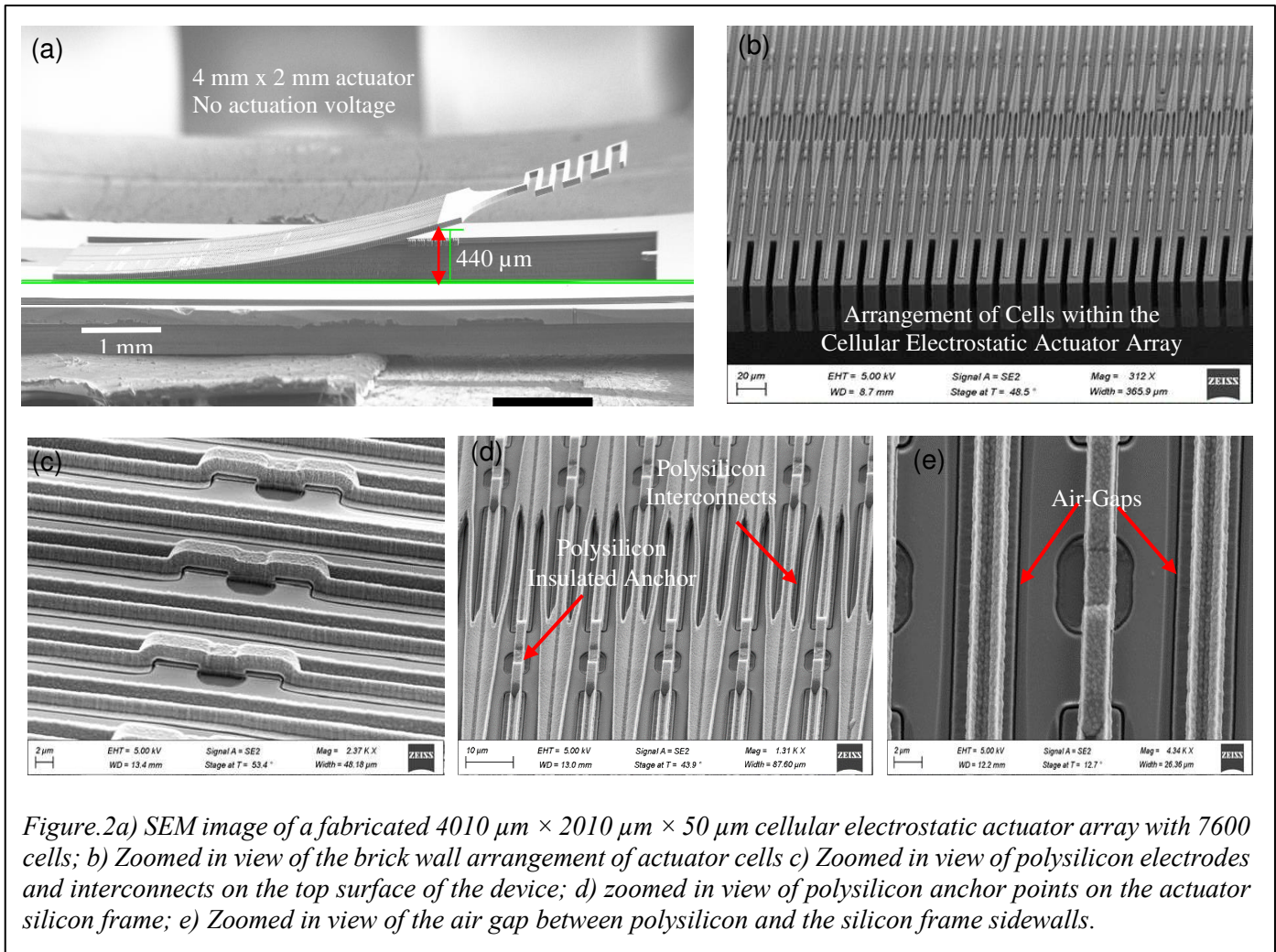


Figure.2a) SEM image of a fabricated  $4010 \mu\text{m} \times 2010 \mu\text{m} \times 50 \mu\text{m}$  cellular electrostatic actuator array with 7600 cells; b) Zoomed in view of the brick wall arrangement of actuator cells c) Zoomed in view of polysilicon electrodes and interconnects on the top surface of the device; d) zoomed in view of polysilicon anchor points on the actuator silicon frame; e) Zoomed in view of the air gap between polysilicon and the silicon frame sidewalls.

287 flexible suspended polysilicon interconnects,  
 288 their anchoring points to the silicon frame, and  
 289 the air gaps are shown in Figures 2b-e. Each cell  
 290 is  $95 \mu\text{m}$  long (trench length of  $80 \mu\text{m}$ ) and  $8 \mu\text{m}$   
 291 wide (trench width of  $5 \mu\text{m}$ ). The transduction  
 292 air-gap between the crystalline silicon sidewalls  
 293 and polysilicon electrodes is around  $250 \text{ nm}$ .  
 294 Due to the residual stress in various deposited  
 295 thin films forming the device, the array is  
 296 curved upward with its tip raised above the  
 297 surface without application of any actuation  
 298 voltage.

299 In order to characterize the performance of the  
 300 actuators, DC tests were performed inside the  
 301 SEM chamber with different DC actuation  
 302 voltages applied between the silicon mesh and  
 303 the polysilicon electrode network. As expected,  
 304 the array curves further upward due to the  
 305 electrostatic force between the silicon and

306 polysilicon walls. Figure 3(a) shows the SEM  
 307 view of the  $4 \text{ mm} \times 2 \text{ mm}$  actuator array of  
 308 Figure 2 with  $46 \text{ V}$  of actuation voltage being  
 309 applied. The free end of the actuator array is  
 310 around  $\sim 1120 \mu\text{m}$  raised above the substrate  
 311 surface ( $\sim 680 \mu\text{m}$  vertical displacement  
 312 compared to its rest position shown in Figure  
 313 2a). Furthermore, a silicon chip with mass of  $8$   
 314  $\text{mg}$  was used to observe the weight lifting and  
 315 throwing capability of the actuator. Figure 3 (b)  
 316 shows the actuator lifting the  $8 \text{ mg}$  weight,  
 317 which is about  $60\text{X}$  times heavier than the  
 318 actuator itself. The weight is lifted by around  
 319  $200 \mu\text{m}$  (visually estimated) with actuation  
 320 voltage of  $45 \text{ V}$ . Further lifting was not possible  
 321 due to the mass rolling and falling off of the  
 322 actuator surface. Figure 3(c) and 3(d) shows the  
 323 SEM image of a  $2 \text{ mm} \times 1 \text{ mm}$  device before  
 324 actuation and upon actuation at  $45 \text{ V}$ . The  $2 \times 1$

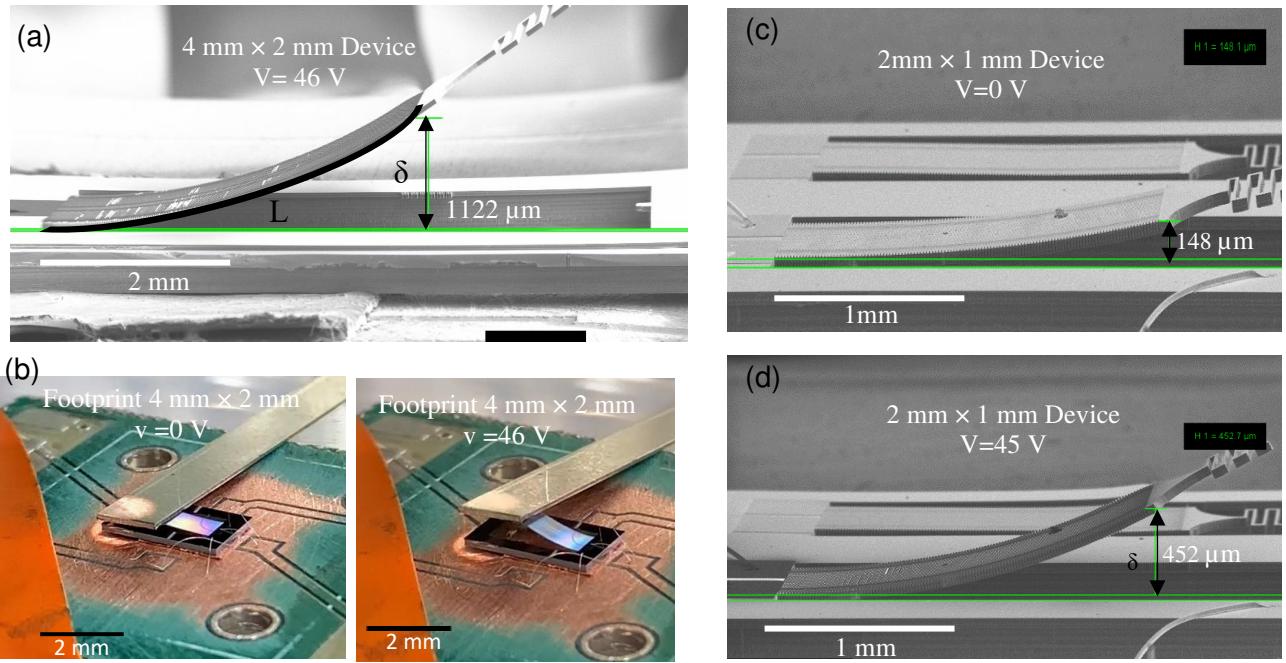


Figure.3a) SEM image of the actuator with foot print of 4 mm×2 mm bent upwards upon the application of actuation voltage 46 V). b) Showing a lifted mass with 45 V actuation voltage. c), d) SEM image of 2 mm×1 mm device before and after actuation.

325 mm<sup>2</sup> array is comprised of 242 rows and 9 or 10  
 326 cells per row in alternative rows (total of 2299  
 327 cells) with individual cell size of 80 μm by 11  
 328 μm. Vertical deflection of up to 304 μm was  
 329 measured for this device with 45 V of actuation  
 330 voltage.

331 The radius of curvature of such structure can be  
 332 calculated based on the array dimensions and  
 333 the displacement at its free end. The equation  
 334 for radius of curvature R for such a structure is:

$$R = \frac{L}{\theta} \quad (1)$$

$$\delta = (1 - \cos\theta)R \quad (2)$$

337 where  $\delta$  is the measured displacement of the  
 338 actuator tip,  $L$  is the length of the actuator and  $\theta$   
 339 is the arch angle of the device. The radius of  
 340 curvature of such bending beam for the 4 mm ×  
 341 2 mm device upon the application of 46 V is  
 342 calculated to be 11.8 mm (around 19° arch  
 343 angle). To achieve such curvature, the array  
 344 should have shrunk by 20 μm on its top surface,  
 345 i.e. each of the airgaps in each cell should have  
 346 shrunk by ~82 nm on the top (155 nm remaining  
 347 airgap). The graph in Figure 4(a) shows the  
 348 measured displacement at the free end of the

349 three different arrays with different actuation  
 350 voltages. Finite element analysis results  
 351 obtained from COMSOL electromechanics  
 352 physics are also plotted on the  
 353 graph of Figure 4(a) showing acceptable  
 354 agreement between measurements and FEA  
 355 given the many sources of potential error (e.g.  
 356 dimensional inaccuracies, sidewall thickness  
 357 variations along the trench thickness, built in  
 358 film stress, etc.).

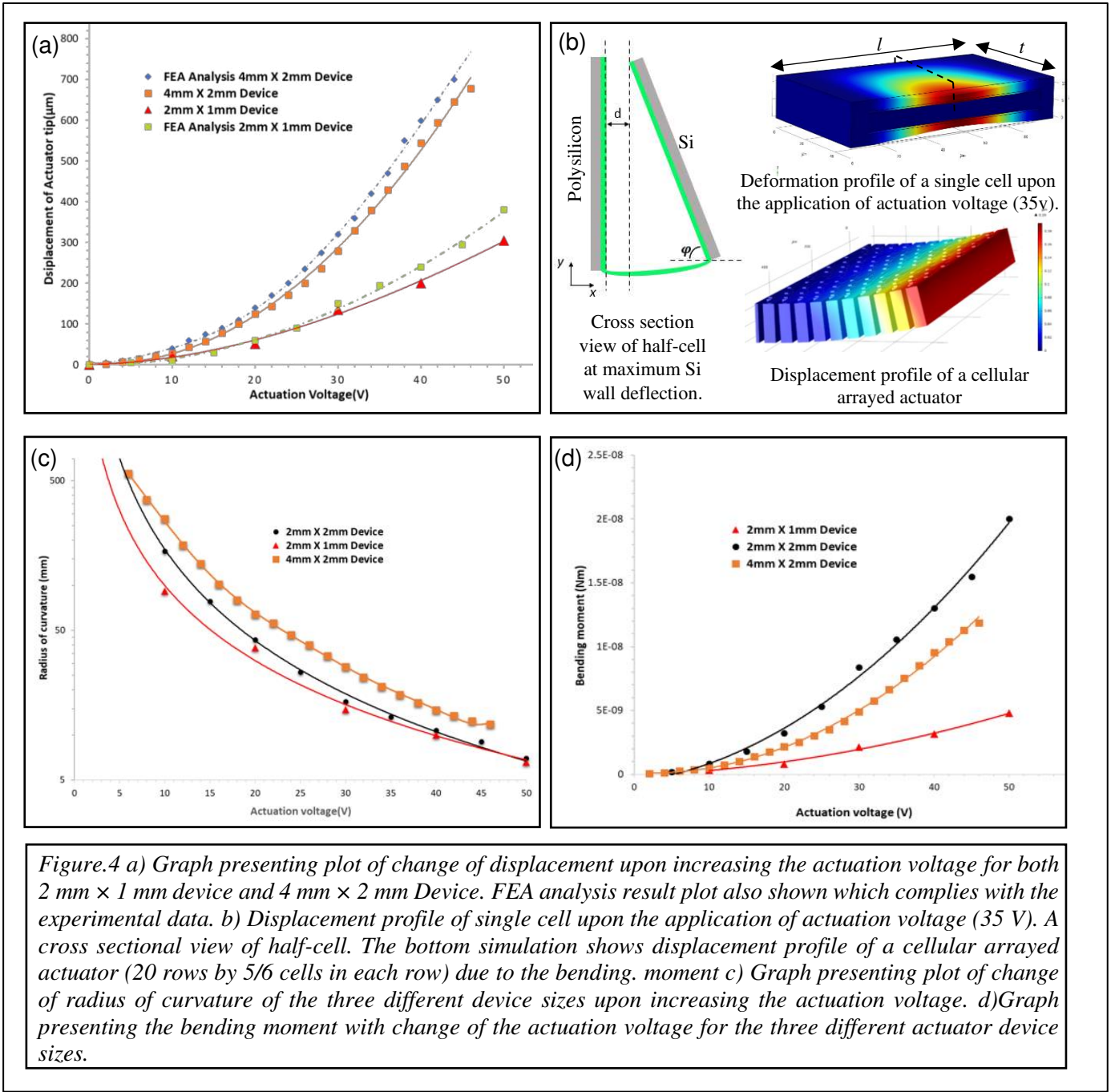
359 The force equation for parallel plate actuators  
 360 with

361 dielectric covered sidewalls is given by:

$$F_{elec,pp} = n \frac{\epsilon_0 A V_{act}^2}{2(g + \frac{t_{di}}{\epsilon_r})^2} \quad (3)$$

363 where  $\epsilon_0$  is the permittivity of air ( $8.85 \times 10^{-12}$   
 364 F/m),  $A$  is the electrode area,  $V_{act}$  is the actuation  
 365 voltage,  $g$  is the air-gap width,  $t_{di}$  and  $\epsilon_r$ , are the  
 366 dielectric thickness and relative permittivity  
 367 respectively, and  $n$  is the number of cells acting  
 368 in each row.

369 In case of the designed actuators, there is a  
 370 gradual change of gap size that happens along  
 371 the cell from the top to the bottom (Figure 4b).



372 Considering this changing gap size, to estimate  
 373 the force in each cell, the following equation is  
 374 used:

$$375 \quad F = \int_0^t \frac{\epsilon \cdot l \cdot y \cdot V_{act}^2}{2(d + y(\cotan \varphi))^2} dy \quad (4)$$

376 where  $t$  is the device thickness,  $d$  is the final  
 377 airgap,  $l$  is the length of the electrode,  $y$  is the  
 378 width of the electrode,  $\varphi$  is the bending angle  
 379 between the polysilicon electrode and the bent  
 380 silicon wall with respect to the  $y$  axis as shown  
 381 in the figure 4(d). The electrostatic force acting

382 on the sidewalls of each cell is calculated to be  
 383 around 1.5 mN with actuation voltage of 46 V.

384 In order to facilitate analysis and predict  
 385 mechanical specifications of actuator designs  
 386 with different dimensions, effective Young's  
 387 modulus is defined for the actuator arrays.  
 388 Effective Young's modulus is the Young's  
 389 modulus required for a structural material  
 390 forming a solid cantilever with the same  
 391 dimensions as the actuator array to have the  
 392 same mechanical stiffness as that of the actuator

393 array. To estimate the effective Young's  
 394 modulus of such complex structure, finite  
 395 element analysis (FEA) using COMSOL solid  
 396 mechanic physics, was performed. A model of  
 397 the actuator array including both the silicon  
 398 frame and polysilicon electrode network was  
 399 created in COMSOL as shown in Figure 4(b).  
 400 The flexural stiffness of the 4 mm × 2mm  
 401 actuator structure was found to be 1.8 N/m at the  
 402 free end of the array by applying a point load to  
 403 the free end and determining the resulting  
 404 displacement. This stiffness was then compared  
 405 to the stiffness of a solid monolithic clamped-  
 406 free cantilever with similar dimensions using  
 407 the following equation:

$$k = \frac{Ewt^3}{4l^3} \quad (5)$$

409 In this manner, the effective Young's modulus  
 410 of the composite structure is calculated to be  
 411 300MPa for the 2mm × 1 mm device and 675  
 412 MPa for the 2mm × 2 mm device. The bending  
 413 moment of the curved structure due to  
 414 electrostatic force acting between the silicon  
 415 mesh and the polysilicon network can be  
 416 obtained from the equation:

$$M = \frac{E_{eff} I}{R} \quad (6)$$

418 where the  $I$  is the moment of inertia,  $E_{eff}$  is the  
 419 effective young's modulus of the fabricated  
 420 device, and  $R$  is the radius of curvature.

421 Knowing the effective young's modulus and the  
 422 radius of curvature obtained using  
 423 measurements and equation (1) and (2), the  
 424 bending moment for the tested device (4 mm ×  
 425 2 mm device) was calculated to be 1.1 μNm  
 426 with 46 V of actuation.

427 To find the energy output of the actuator, the  
 428 following equation can be used <sup>21</sup>:

$$U = \frac{M\theta}{2} \quad (7)$$

430 where  $M$  is the bending moment, and  $\theta$  is the  
 431 arch angle (19 degrees in this case). This leads  
 432 to total output energy of 0.19 μJ for the tested  
 433 actuator that translates to energy density per  
 434 volume of .47 mJ/cm<sup>3</sup>. Figures 4(c) shows the  
 435 graph for radius of curvature versus the  
 436 actuation voltage, and figure 4(d) shows the  
 437 bending moment versus the actuation voltage  
 438 for the three tested prototypes with different cell  
 439 dimensions and overall footprints. The 2 × 2  
 440 mm<sup>2</sup> actuator array exhibited up to 332 μm  
 441 vertical displacement with 60 V actuation  
 442 voltage. This device provides energy density of

Table.1 Showing parameters of three tested devices along with their measured performance.

Device Footprint	2mm × 1mm	2mm × 2mm	4mm × 2mm
Cell length	80 μm	80 μm	80 μm
Side wall width	3 μm	4 μm	4 μm
Polysilicon electrode width	5 μm	7 μm	7 μm
Device layer thickness	50 μm	50 μm	50 μm
Vertical displacement upon actuation voltage	304 μm	333 μm	678 μm
Actuation Voltage	45 V	60 V	46 V
Flexural stiffness of device	3.4 N/m	14.2 N/m	1.8N/m
Effective Young's Modulus	301 MPa	675 MPa	675 MPa
Bending moment	4.7×10 <sup>-7</sup> Nm	2.0×10 <sup>-6</sup> Nm	1.1×10 <sup>-6</sup> Nm
Radios of curvature	6.56 mm	6.93 mm	11.8 mm
Energy density	0.7 mJ/cm <sup>3</sup>	1.42 mJ/cm <sup>3</sup>	0.47 mJ/cm <sup>3</sup>

443 1.42 mJ/cm<sup>3</sup>, which is the highest measured  
 444 among the three prototypes tested.  
 445 Table 1 summarizes the specifications and tests  
 446 results for the three different tested actuators.

## 447 DISCUSSION

448 Displacement range of the movable  
 449 electrode in a parallel plate electrostatic actuator  
 450 is limited to the transduction gap between the  
 451 electrodes. The presented cellular actuators are  
 452 able to bypass this limitation and allow  
 453 realization of electrostatic actuators with both  
 454 high energy density (submicron transduction  
 455 gaps) and large displacements. This reinforces  
 456 the idea of cascading individual cells to form the  
 457 arrayed cell structures. The fabricated actuator  
 458 has shown a maximum displacement of 678 μm  
 459 and maximum energy density of 1.42 mJ/cm<sup>3</sup>.  
 460 Table 2 shows a summary of performance of the  
 461 tested devices compared to some of the existing  
 462 relevant work in the literature showing  
 463 significantly higher energy density,  
 464 displacement, and output force with a relatively  
 465 low actuation voltage.

466 A limiting factor for the presented devices is  
 467 the breakdown that occurs at significantly lower  
 468 than expected voltages. The maximum  
 469 achievable force, displacement, and energy  
 470 density is proportional to the square of the

471 maximum actuation voltage that can be safely  
 472 applied to the device without electrical  
 473 breakdown. With a 500 nm thick silicon nitride  
 474 film as the dielectric ( $\epsilon_r = 8$ ) and air-gap of 500  
 475 nm, the maximum estimated actuation voltage  
 476 is supposed to be around 140V while the  
 477 fabricated devices exhibit breakdown voltages  
 478 below 60 V during testing. By mitigating this  
 479 problem in future processes, energy density as  
 480 high as 13 mJ/cm<sup>3</sup> is expected to be achievable.

## 481 CONCLUSION

482 Micromachined electrostatic cellular  
 483 actuators with submicron high aspect ratio  
 484 transduction air-gaps were fabricated and  
 485 characterized. Vertical displacement of around  
 486 678 μm for the 4 mm × 2 mm device at 46 V  
 487 and energy density of 1.42 mJ/cm<sup>3</sup> was  
 488 measured for the 2 mm × 2 mm actuator. Early  
 489 breakdown of the wire bond pads was an issue  
 490 that need to be further studied. The longterm  
 491 reliability and durability test study would give  
 492 more insight on further improving the  
 493 performance of the actuator. Prolonged  
 494 durability of the actuator components  
 495 (especially the sidewall dielectric film) under  
 496 millions to billions of full actuation cycles with  
 497 potential physical contact between the sidewalls  
 498 would give insight on the mechanical viability

*Table.2 Out of plane performance of the arrayed cellular actuator compared to some of the other works recently reported in this area of research.*

	Force	Displacement	Energy Density	Actuation voltage
Electrostatic Piston tube Actuator <sup>20</sup>	59μN	28μm	0.178μJ/cm <sup>3</sup> *	80V
Zipper Microstage actuator <sup>25</sup>	32μN	212μm	1.186mJ/cm <sup>3</sup> *	135V
Repulsive actuator for large out-of-plane force <sup>26</sup>	40μN	15μm	NR **	120V
PZT actuator with MEMs enabled motion amplifier <sup>27</sup>	5.3mN	3.3μm	0.02mJ/cm <sup>3</sup> *	170V
Nanoelectrostatic Drive(NED) actuator <sup>21</sup>	NR **	226nm	NR **	45V
Low Voltage Electrostatic Micro actuator <sup>28</sup>	0.37μN	58μm	NR**	25V
Electrostatic MEMS spring actuator <sup>29</sup>	NR**	2.7μm	NR**	50V
<b>Arrayed cellular Electrostatic actuator</b>	<b>80mN</b>	<b>678μm</b>	<b>1.42mJ/cm<sup>3</sup></b>	<b>46V</b>

\* Calculated by the authors from provided information

\*\* Not reported

499 of the actuator. Endurance of the giant electric  
 500 field between the narrow air-gaps and the  
 501 dielectric films covering the gap sidewalls over  
 502 the long lifetime of the actuator and millions of  
 503 operating cycles is also an important factor for  
 504 improving further performance output of the  
 505 designed actuator.

506 **MATERIALS AND METHODS**

507 *ACTUATOR FABRICATION:*

508 Figure 5 shows the cross-sectional schematic  
 509 view of the process flow used for fabrication of  
 510 the described cellular actuator arrays on silicon  
 511 on insulator (SOI) substrates using the modified  
 512 version of the High Aspect-Ratio Polysilicon  
 513 and Silicon (HARPSS) fabrication process [23].  
 514 The process starts by deep reactive ion etching  
 515 (DRIE) of vertical trenches into the silicon  
 516 device layer (50µm thick) of the SOI substrate.  
 517 Trenches extend all the way through the device  
 518 layer to the SOI buried oxide layer (BOX)

519 (Figure 5(a). This step defines the crystalline  
 520 silicon mesh of the actuators keeping the silicon  
 521 device layer around the actuator intact (the mesh  
 522 is still part of the surrounding device layer).

523 A thermal oxidation and oxide removal step is  
 524 than performed to remove the surface roughness  
 525 (scalloping and striations) induced on the  
 526 silicon sidewalls during deep silicon etch to  
 527 form the trench. A conformal layer low stress  
 528 silicon nitride was then deposited via LPCVD  
 529 covering the sidewalls. This was followed by a  
 530 layer of conformal silicon dioxide deposited via  
 531 LPCVD serving as the sacrificial layer defining  
 532 the transduction air-gap between the crystalline  
 533 silicon sidewalls and polysilicon electrodes  
 534 (Figure 5(b)). A 3.5 µm thick layer of LPCVD  
 535 p-doped polysilicon was then deposited to refill  
 536 the trenches and form the vertical electrodes  
 537 within the cells (Figure 5(c)). Polysilicon was  
 538 then blanket etched on the top surface (Figure

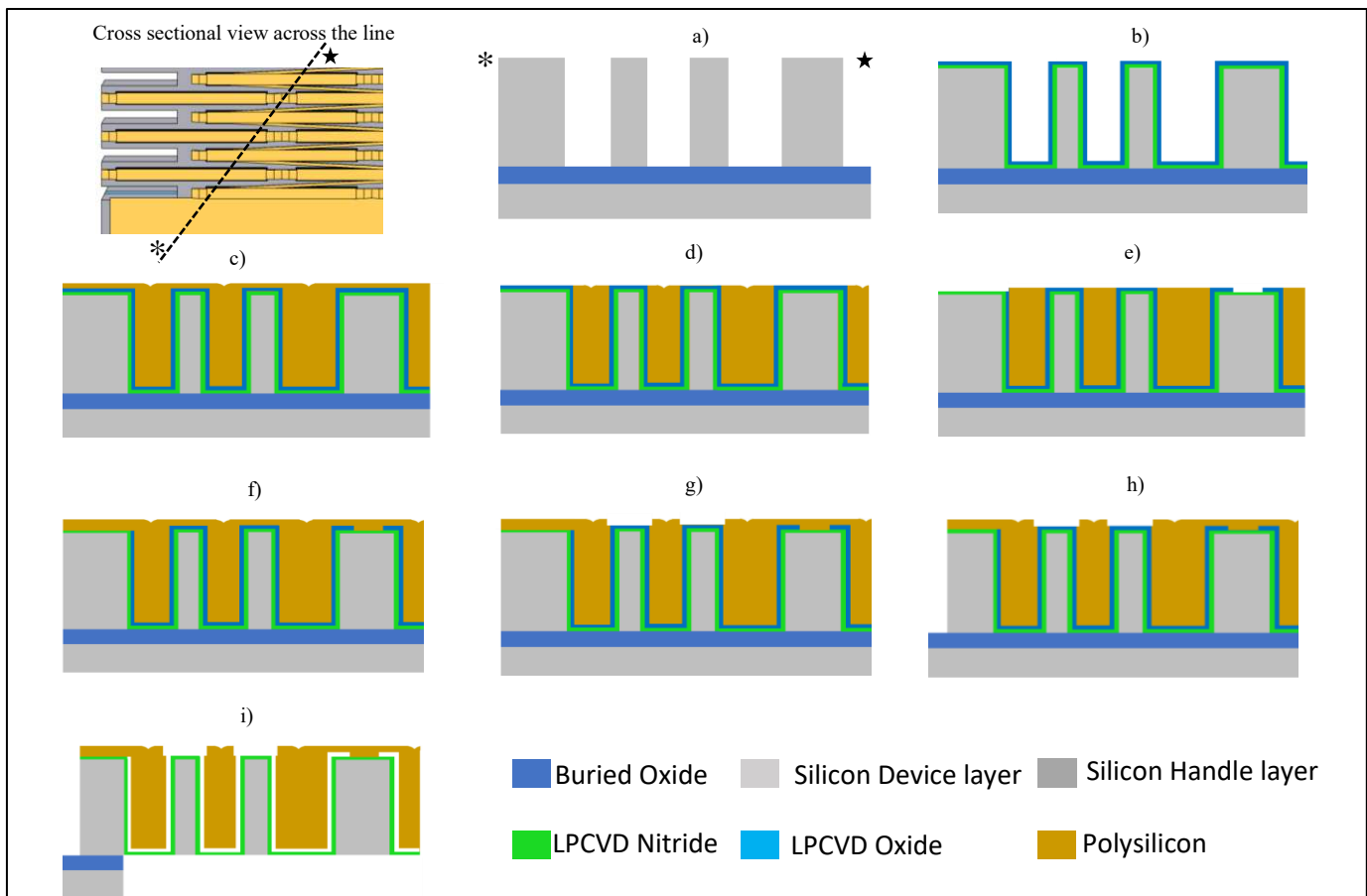


Figure.5 Schematic showing cross-sectional view of the modified HARPSS micromachining process flow used for fabrication of the high-output cellular electrostatic actuator arrays.

539 5(d)) providing access to the underlying  
540 sacrificial silicon dioxide layer. The 2<sup>nd</sup>  
541 lithography steps was then performed  
542 selectively to remove the oxide film from  
543 certain areas where the electrodes are to be  
544 anchored onto the silicon mesh (Figure 5(e)). A  
545 second layer of doped LPCVD polysilicon (1.5  
546  $\mu\text{m}$  Thick) was then deposited (Figure 5(f)).  
547 After this, annealing at 1100 degree is done that  
548 improves the resistivity of the polysilicon. The  
549 2<sup>nd</sup> polysilicon is then patterned (the 3<sup>rd</sup>  
550 lithography step) forming interconnects  
551 between polysilicon electrodes and electrode  
552 anchors to the silicon frame (at nodal points  
553 where deformation of the frame is close to zero).  
554 The underlying nitride layer provides electrical  
555 isolation between the anchored polysilicon and  
556 silicon mesh. Processing continued by plasma  
557 etching the second polysilicon layer (Figure  
558 5(g)). Another topside lithography step was then  
559 performed to pattern the silicon device layer  
560 around the actuator arrays defining the outline  
561 of the devices as well as forming the supporting  
562 tethers (Figure 5(h)). The actuators have  
563 relatively large sizes in the few millimeters  
564 range, therefore, to avoid stiction and minimize  
565 the time required to undercut the silicon  
566 structures (during BOX layer removal at the end  
567 of the process), the silicon handle layer  
568 underneath the arrays is to be removed. For this  
569 purpose, a backside lithography step followed  
570 by a long through handle layer DRIE is  
571 performed. Finally, the sacrificial oxide  
572 between the nitride covered silicon and  
573 polysilicon sidewalls within the deep trenches  
574 was removed by a 10-minute-long dip in 49%  
575 hydrofluoric acid (HF) solution (Figure 5(i)).  
576 Silicon nitride has a very low etch rate in HF  
577 and therefore, most of the thickness of the  
578 nitride layer covering the silicon sidewalls is  
579 expected to remain in place.

## 580 REFERENCES

581 [1] Karpelson, M., Wei, G. Y., & Wood, R. J. (2008,  
582 May). A review of actuation and power electronics  
583 options for flapping-wing robotic insects. In *2008 IEEE*  
584 *international conference on robotics and automation* (pp.  
585 779-786). IEEE.

586 [2] Liu, X., Kim, K. and Sun, Y., 2007. A MEMS stage  
587 for 3-axis nanopositioning. *Journal of Micromechanics*  
588 *and Microengineering*, 17(9), p.1796.

589 [3] Gutierrez, R. C., Tang, T. K., Calvet, R., & Fossum,  
590 E. R. (2007, February). MEMS digital camera. In *Digital*  
591 *Photography III* (Vol. 6502, p. 65020K). International  
592 Society for Optics and Photonics.

593 [4] Nisar, Asim, Nitin Afzulpurkar, Banchong  
594 Mahaisavariya, and Adisorn Tuantranont. "MEMS-based  
595 micropumps in drug delivery and biomedical  
596 applications." *Sensors and Actuators B: Chemical* 130,  
597 no. 2 (2008): 917-942.

598 [5] Yalcinkaya, A. D., Urey, H., Brown, D., Montague,  
599 T., & Sprague, R. (2006). Two-axis electromagnetic  
600 microscanner for high resolution displays. *Journal of*  
601 *Microelectromechanical Systems*, 15(4), 786-794.

602 [6] Bell, D. J., Lu, T. J., Fleck, N. A., & Spearing, S. M.  
603 (2005). MEMS actuators and sensors: observations on  
604 their performance and selection for purpose. *Journal of*  
605 *Micromechanics and Microengineering*, 15(7), S153.

606 [7] Liu, Daniel Kuang-Chen, James Friend, and Leslie  
607 Yeo. "A brief review of actuation at the micro-scale using  
608 electrostatics, electromagnetics and piezoelectric  
609 ultrasonics." *Acoustical Science and Technology* 31, no.  
610 2 (2010): 115-123.

611 [8] Filhol, F., Defay, E., Divoux, C., Zinck, C., & Delaye,  
612 M. T. (2005). Resonant micro-mirror excited by a thin-  
613 film piezoelectric actuator for fast optical beam  
614 scanning. *Sensors and Actuators A: Physical*, 123, 483-  
615 489.

616 [9] Michael, A., Kwok, C. Y., Yu, K., & Mackenzie, M.  
617 R. (2008). A novel bistable two-way actuated out-of-  
618 plane electrothermal microbridge. *Journal of*  
619 *microelectromechanical systems*, 17(1), 58-69.

620 [10] Xu, Y., Singh, J., Selvaratnam, T., & Chen, N.  
621 (2009). Two-axis gimbal-less electrothermal micromirror  
622 for large-angle circumferential scanning. *IEEE Journal of*  
623 *Selected Topics in Quantum Electronics*, 15(5), 1432-  
624 1438.

625 [11] Wen, M., Luo, Z., Wang, W., & Liu, S. (2014,  
626 August). A characterization of the performance of MEMS  
627 vibratory gyroscope in different fields. In *2014 15th*  
628 *International Conference on Electronic Packaging*  
629 *Technology* (pp. 1547-1551). IEEE.

630 [12] Wang, Y., Zhang, J., Yao, Z., Lin, C., Zhou, T., Su,  
631 Y. and Zhao, J., 2018. A MEMS resonant accelerometer  
632 with high performance of temperature based on

- 633 electrostatic spring softening and continuous ring-down  
634 technique. *IEEE Sensors Journal*, 18(17), pp.7023-7031.
- 635 [13] Zehnder, A.T., Rand, R.H. and Krylov, S., 2018.  
636 Locking of electrostatically coupled thermo-optically  
637 driven MEMS limit cycle oscillators. *International*  
638 *Journal of Non-Linear Mechanics*, 102, pp.92-100.
- 639 [14] Fraser, John Douglas. "Capacitive micromachined  
640 ultrasonic transducers." U.S. Patent 6,443,901, issued  
641 September 3, 2002.
- 642 [15] Paschen, 1889 Wied. Ann 37, pp. 69-96.
- 643 [16] P. L. Chapman and P. T. Krein, "Micromotor  
644 technology: electric drive designer's perspective," in  
645 *Conference Record of the 2001 IEEE Industry*  
646 *Applications Conference, 2001*. Thirty-Sixth IAS Annual  
647 Meeting, 2001, vol. 3, pp. 1978-1983 vol.3.
- 648 [17] A. J. Wallash, and L. Levit, "Electrical breakdown  
649 and ESD phenomena for devices with nanometer to  
650 micron gaps," *proceedings of SPIE, Micromachining and*  
651 *Microfabrication, 2003*, pp. 87-96.
- 652 [18] Hou, Max Ti-Kuang, Gordon Kou-Wei Huang,  
653 Jing-Yi Huang, Ke-Min Liao, Rongshun Chen, and Jer-  
654 Liang Andrew Yeh. "Extending displacements of comb  
655 drive actuators by adding secondary comb electrodes."  
656 *Journal of micromechanics and microengineering* 16, no.  
657 4 (2006): 684.
- 658 [19] Yeh, Richard, Seth Hollar, and Kristofer SJ Pister.  
659 "Single mask, large force, and large displacement  
660 electrostatic linear inchworm motors." *Journal of*  
661 *Microelectromechanical Systems* 11, no. 4 (2002): 330-  
662 336.
- 663 [20] Ba-Tis, Faez, and Ridha Ben-Mrad. "A 3-DOF  
664 MEMS electrostatic piston-tube actuator." *Journal of*  
665 *Microelectromechanical Systems* 24, no. 4 (2015): 1173-  
666 1184.
- 667 [21] Conrad, Holger, Harald Schenk, Bert Kaiser, Sergiu  
668 Langa, Matthieu Gaudet, Klaus Schimmanz, Michael  
669 Stolz, and Miriam Lenz. "A small-gap electrostatic  
670 micro-actuator for large deflections." *Nature*  
671 *communications* 6, no. 1 (2015): 1-7.
- 672 [22] Abbasalipour, Amin, Prithviraj Palit, and Siavash  
673 Pourkamali. "High-Energy Density Micro-Machined  
674 Cellular Arrays of Electrostatic Actuators." In 2019 *20th*  
675 *International Conference on Solid-State Sensors,*  
676 *Actuators and Microsystems & Eurosensors XXXIII*  
677 (TRANSDUCERS & EUROSensors XXXIII), pp.  
678 1870-1873. IEEE, 2019.
- 679 [23] S. Pourkamali, Z. Hao and F. Ayazi, "VHF  
680 single crystal silicon side supported disk resonators-Part  
681 II: implementation and characterization," *Journal of*  
682 *Micro Electro Mechanical Systems*, Vol. 13, Issue 6,  
683 December 2004, pp. 1054-1062.
- 684 [24] A. J. Wallash, and L. Levit, "Electrical breakdown  
685 and ESD phenomena for devices with nanometer to  
686 micron gaps," *proceedings of SPIE, Micromachining and*  
687 *Microfabrication, 2003*, pp. 87-96.
- 688 [25] Felder, J., Lee, E., & DeVoe, D. L. (2014). Large  
689 vertical displacement electrostatic zipper microstage  
690 actuators. *Journal of Microelectromechanical*  
691 *Systems*, 24(4), 896-903.
- 692 [26] Khan, I., & Mrad, R. B. (2014). Development of a  
693 MEMS repulsive actuator for large out-of-plane  
694 force. *Journal of Micromechanics and*  
695 *Microengineering*, 24(3), 035022.
- 696 [27] Xie, X., & Livermore, C. (2015, November). A high-  
697 force, out-of-plane actuator with a MEMS-enabled  
698 microscissor motion amplifier. In *Journal of Physics:*  
699 *Conference Series* (Vol. 660, No. 1, p. 012026). IOP  
700 Publishing
- 701 [28] Towfighian, S., He, S., & Ben Mrad, R. (2014). A  
702 low voltage electrostatic micro actuator for large out-of-  
703 plane displacement. In *ASME 2014 International Design*  
704 *Engineering Technical Conferences and Computers and*  
705 *Information in Engineering Conference*. American  
706 Society of Mechanical Engineers Digital Collection.
- 707 [29] Hu, F., Wang, W., & Yao, J. (2011). An electrostatic  
708 MEMS spring actuator with large stroke and out-of-plane  
709 actuation. *Journal of Micromechanics and*  
710 *Microengineering*, 21(11), 115029.

## Supplementary Files

This is a list of supplementary files associated with this preprint. Click to download.

- [SupplementaryVideos.rar](#)